Iron(III) fluoride synthesized by a fluorolysis method and its electrochemical properties as a positive electrode material for lithium secondary batteries

Shinya Tawa, Takayuki Yamamoto, Kazuhiko Matsumoto*, Rika Hagiwara

Graduate School of Energy Science, Kyoto University, Yoshida-honmachi, Sakyo-ku, Kyoto 606-8501, Japan

*Corresponding author

E-mail: k-matsumoto@energy.kyoto-u.ac.jp (K. Matsumoto)

Tel: +81-75-753-5827

Fax: +81-75-753-5906

Key words**:** Iron(III) fluoride, Lithium secondary battery, Fluorolysis method, Positive electrode

Abstract

Iron(III) fluoride (FeF_3) with low crystallinity and high surface area has been synthesized by a fluorolysis method, and applied as a positive electrode material for lithium secondary batteries. The FeF_3 prepared with a high molar ratio of hydrogen fluoride exhibits a high surface area and crystallinity. The FeF_3 sample treated at 300 °C under a F_2/Ar atmosphere exhibits the highest surface area and was selected for further electrochemical test in view of improvement of performance in the potential region of conversion reactions. The initial discharge (lithiation) capacity was 676 mAh g^{-1} that was close to the theoretical capacity of FeF_3 (712 mAh g^{-1}). Compared to the highly crystalline FeF_3 commercially available, the synthesized FeF_3 in the present study exhibited a low discharge capacity attributed to the insertion reaction because of the low crystallinity, and showed a low overpotential and larger capacity corresponding to the conversion reaction owing to the higher surface area of the fluorides.

1. Introduction

Lithium ion batteries (LIBs) are widely used for various kinds of portable electronic devices such as mobile phones and laptop computers due to their high energy densities. Large-scaled LIBs are also developed for electric vehicles (EVs), hybrid electric vehicles (HEVs), and stationary use[1-3]. A new positive electrode material with large capacity is needed for these devices, because current positive electrode materials utilize insertion reactions with intrinsically limited capacities based on one- (or less) electron reaction per formula unit (140 mAh g^{-1} for $LiCoO_2$ (0.5 Li) [4,5] and 170 mAh g^{-1} for $LiFePO_4$ (1 Li) [6]). Thus, instead of such insertion materials, iron(III) fluoride (FeF_3) has been receiving attention as a positive electrode material with a high theoretical capacity of 712 mAh g^{-1} based on the three-electron reaction, reasonably high average operating potential of 2.7 V vs. Li^+/Li, in addition to abundant resources of iron [7–26].

In the first report on charge–discharge behavior by Arai et al. in 1997 [7], FeF_3 showed a small capacity of 80 mAh g^{-1} corresponding to the reaction of only 0.5 Li per formula unit. The limited capacity arose from the poor electronic conductivity of FeF_3 owing to the large bandgap induced by the highly ionic character of the Fe–F bonds. This insulating problem was improved by ball-milling with carbon materials and, in some reports, high reversible capacities of ca. 600 mAh g^{-1} were attained according to the two consecutive reactions [8,9];

$$FeF_3 + Li^+ + e^- \rightleftarrows LiFeF_3 \quad (1)$$

$$LiFeF_3 + 2\ Li^+ + 2\ e^- \rightleftarrows Fe + 3\ LiF \quad (2)$$

In the discharging process, the first reaction (Eq. (1)) occurs in a potential region of 2.0–4.5 V vs. Li^+/Li, corresponding to the lithium insertion into the FeF_3 framework. The second reaction (Eq. (2)) is a conversion reaction that occurs in a potential region of 1.0–2.0 V vs. Li^+/Li.

Despite its high theoretical capacity, several drawbacks such as large overpotential, poor capacity retention, and poor rate capability have prevented FeF_3 from its practical application as a positive electrode material. These drawbacks are caused by the intrinsic poor electronic

conductivity of FeF_3 and structural degradation during the conversion reaction. Several groups have investigated the performance of FeF_3 positive electrodes to overcome these drawbacks. Yabuuchi et al. reported that FeF_3 with higher crystallinity showed good capacity retention and rate capability by utilizing only the insertion/desertion reaction [15]. However, the obtained capacities were less than the theoretical capacity for one electron reaction (237 mAh g^{-1}). In other cases involving conversion reaction, no satisfactory results have been achieved especially in terms of rate and cycling performance. In order to improve the performances for the conversion reaction, it is favorable to shorten and increase the lithium insertion pathways and to create the abundant active reaction area for FeF_3 and lithium. Thus, the authors focused on the fluorolysis method to prepare metal fluorides with high surface area [27].

The fluorolysis method gives amorphous (or low crystalline) metal fluorides with high surface areas through two consecutive steps. In the first step, a precursor of metal fluoride is prepared by mixing organic solutions of anhydrous hydrogen fluoride (HF) and a metal salt (alkoxides, nitrates, or chlorides) followed by removal of organics *in vacuo*. In the second step, the obtained precursor is fluorinated by a fluorine containing gas at elevated temperatures to form metal fluoride [27-32]. Several studies reported the effects of synthetic conditions on the structural properties of AlF_3 [29] and MgF_2 [30]. Although there is a report on synthesis of FeF_3 by a fluorolysis method under anhydrous conditions [32], detailed effects of synthetic conditions to the product are remained unclear.

In this study, FeF_3 was synthesized by a fluorolysis method under different synthetic conditions in order to investigate the effects of the synthetic conditions on the structural properties of FeF_3 such as crystallinity and surface area. Charge–discharge properties of the FeF_3 product as a positive electrode material for lithium secondary batteries were also evaluated. Although some products may contain residual organic or oxygen containing-groups as mentioned below, the product is mainly regarded as FeF_3 and thus they are called FeF_3 in the present paper.

2. Results and discussion

2.1 FeF_3 precursor, $FeF_{3-x}(acac)_x$

Powdery precursors of FeF_3 were obtained by the reaction of $Fe(acac)_3$ and HF in the different molar ratios of 1:3, 1:5, and 1:7 where 'acac' is acetylacetonate. The precursors are denoted as Pre3, Pre5, and Pre7, respectively. According to the results of elemental analysis as shown in Table 1, C content decreases and F content increases with the increase in HF ratio, suggesting that the nucleophilic substitution of the acetylacetonate group for fluorine proceeds effectively in the reaction condition of high HF ratio. Based on the C and F contents, the x value in $FeF_{3-x}(acac)_x$ is calculated to be 1.0, 0.5, and 0.4 for Pre3, Pre5, and Pre7, respectively. The substitution reaction is particularly retarded for Pre3 compared with the other precursors. X-ray diffraction (XRD) patterns of the precursors are shown in Fig. 1. Although Pre3 and Pre5 are amorphous, Pre7 is slightly crystalline, exhibiting one weak XRD diffraction peak around 2θ = 24° attributable to the 012 diffraction line of the rhombohedral FeF_3.

Table 1 Results of elemental analysis for the FeF_3 precursors.

Name	Molar ratio of $Fe(acac)_3$:HF	C / wt%	H / wt%	F / wt% [a]	x in $FeF_{3-x}(acac)_x$
Pre3	1:3	29.8	4.2	18.0	1.0
Pre5	1:5	19.4	3.4	29.5	0.5
Pre7	1:7	16.7	3.3	32.0	0.4

[a] Theoretical F content for FeF_3 is 50.5 wt%.

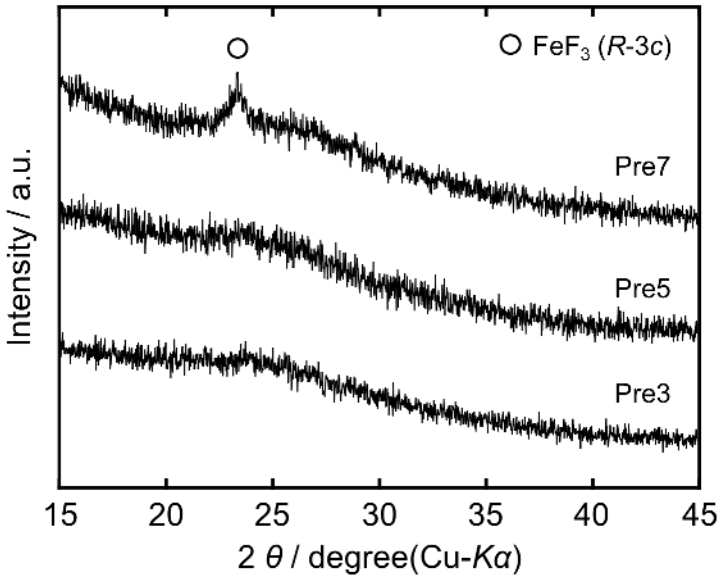

Fig. 1 X-ray diffraction patterns of the FeF_3 precursors. The molar ratio of $Fe(acac)_3$:HF during the synthesis of precursors were 1:3 for Pre3, 1:5 for Pre5, and 1:7 for Pre7.

2.2 FeF_3 product

2.2.1 Effects of HF ratio

In order to investigate the effects of the HF ratio, FeF_3 was prepared through fluorination of the different FeF_3 precursors (Pre3, Pre5, and Pre7) by fluorination at the same temperature of 200 °C under the flow of the F_2/Ar (1/4) gas. The obtained colorless products are denoted as Flu3-200, Flu5-200, and Flu7-200.

Results of elemental analysis for the products are summarized in Table 2. No apparent dependence of the HF ratio for the preparation of the precursor on the elemental ratio was observed for the results of elemental analysis. Although small amounts of carbon impurities derived from the acetylacetonate group remain in all the products, the fluorination reaction proceeded enough to increase the F contents in the products close to the theoretical value for FeF_3 (50.5 wt%). The high F content observed for Flu3-200 could originate from the existence of fluorocarbons formed by the fluorination of the precursor (Pre3) that possesses the higher C content than the other precursors (see Table 1). The XRD patterns of the FeF_3 products are shown in Fig. 2. Although the amorphous

Pre5-200 was fluorinated to form low crystalline Flu5-200 with very weak and broad diffraction peak around 2θ = 24°, Flu3-200 was still amorphous after fluorination at 200 °C. The crystallinity only slightly increased by the fluorination in any case, indicating that crystallinity of the resulting FeF_3 products mainly depends on the HF ratio in the first reaction step.

Nitrogen adsorption–desorption isotherms of the FeF_3 products are shown in Fig. 3a. Higher adsorption capacities are observed for products prepared under the condition of the higher HF ratio, resulting in the higher BET surface area as shown in Table 2. All the isotherms exhibit hysteresis loops, suggesting the existence of mesopores. The degree of hysteresis is the most prominent for Flu7-200, suggesting a large volume of mesopores. Pore size distribution evaluated from the isotherms (Fig. 3b) indicates that the total volume of pores increases as the HF ratio during the synthesis of precursors increases. From these results, it is suggested that the synthetic condition of the higher HF ratio produces FeF_3 with high surface area which could be beneficial for conversion reactions for lithium secondary batteries.

Table 2 Results of elemental analysis and BET surface area of the FeF_3 products.

Name	Molar ratio of $Fe(acac)_3$:HF	C / wt%	H / wt%	F / wt% [a]	BET / $m^2\ g^{-1}$
Flu3-200	1:3	4.7	0.9	50.0	11
Flu5-200	1:5	3.6	1.2	46.5	47
Flu7-200	1:7	4.6	1.7	48.3	74

[a] Theoretical F content for FeF_3 is 50.5 wt%.

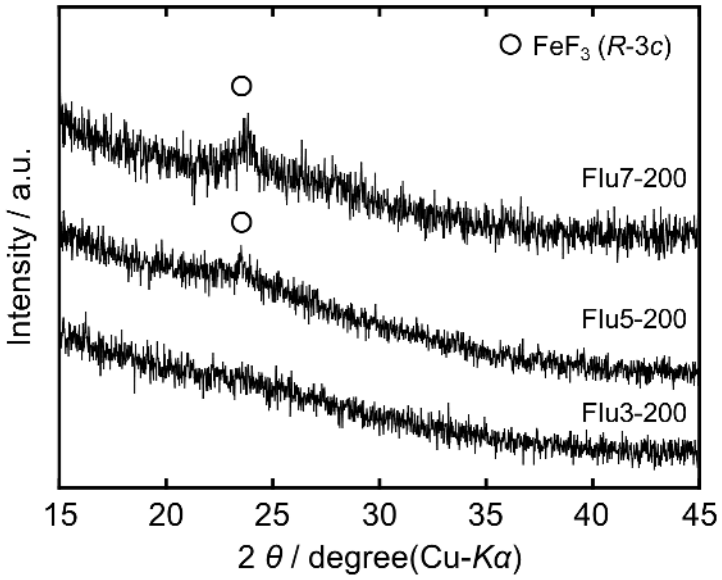

Fig. 2 X-ray diffraction patterns of the FeF_3 products. The molar ratio of $Fe(acac)_3$:HF during the synthesis of precursors were 1:3 for Flu3-200, 1:5 for Flu5-200, and 1:7 for Flu7-200. The fluorination temperature was 200 °C.

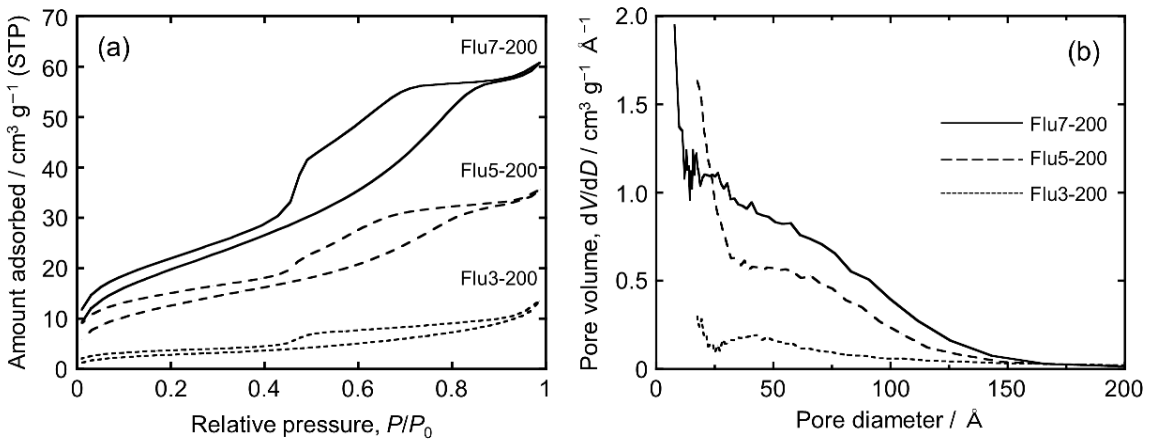

Fig. 3 (a) Nitrogen adsorption–desorption isotherms and (b) pore-size distributions of the FeF_3 products. The molar ratio of $Fe(acac)_3$:HF is 1:3 for Flu3-200, 1:5 for Flu5-200, and 1:7 for Flu7-200. The fluorination temperature is 200 °C.

2.2.2 Effects of fluorination temperature

Effects of fluorination temperature in the second reaction step were investigated for the FeF_3 precursor prepared under the synthetic condition of the highest HF ratio (Pre7) to obtain FeF_3 products of high surface area. In addition to the fluorination temperature (200 °C) adopted in the previous section, two different temperatures of 300 and 400 °C were selected. These FeF_3 samples are denoted as Flu7-200, Flu7-300, and Flu7-400, respectively.

Results of elemental analysis of the FeF_3 products are summarized in Table 3. The high fluorination temperature gives the resulting FeF_3 with low C contents owing to the effective removal of organic groups (the C content of 0.3 wt% for Flu7-400). X-ray diffraction patterns of the products are shown in Fig. 4. In contrast to the HF ratio in the first reaction step (see Fig. 2), little effect of fluorination temperature on crystallinity is observed, indicating that crystallinity of the resulting FeF_3 product is mainly dependent on the HF ratio in the first reaction step. Nitrogen adsorption-desorption isotherms of the FeF_3 products fluorinated at different temperatures are shown in Fig. 5a. All the products show the similar isotherms in shape with large hysteresis loops during adsorption and desorption. These hysteresis loops suggest that the products are highly mesoporous. The Flu7-300 sample shows the highest adsorption capacity, resulting in the highest BET surface area as shown in Table 3. The sharp peak at 3 nm for Flu7-300 in the pore size distribution (Fig. 5b) contributes to the large pore volume and the high surface area of 140 $m^2\ g^{-1}$ for this sample. However, the peak disappears for Flu7-400 owing to the aggregation of particles due to the sintering at high temperature, leading to the lower surface area than that of Flu7-300.

Table 3 Results of elemental analysis and BET surface area of the FeF_3 products.

Name	Fluorination temperature / °C	C / wt%	H / wt%	F / wt% [a]	BET / $m^2\ g^{-1}$
Flu7-200	200	4.6	1.7	48.3	74
Flu7-300	300	2.4	1.7	48.2	140
Flu7-400	400	0.3	1.6	47.3	101

[a] Theoretical F content for FeF_3 is 50.5 wt%.

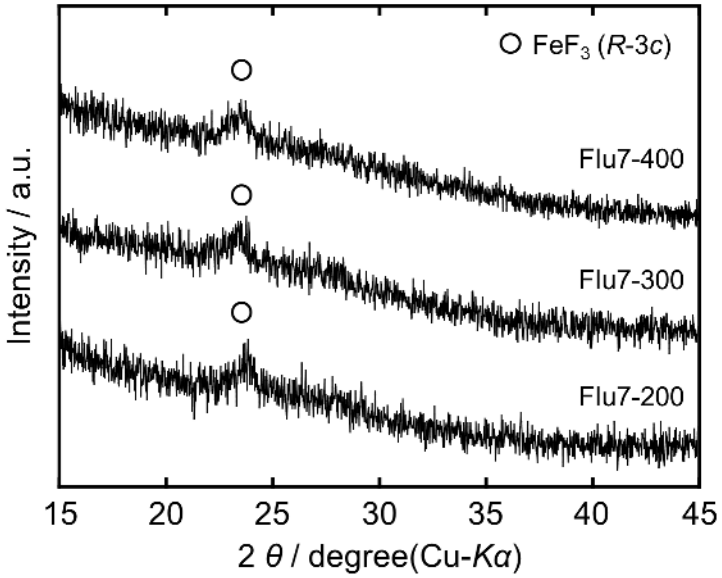

Fig. 4 X-ray diffraction patterns of the FeF_3 products. The fluorination temperature was 200 °C for Flu7-200, 300 °C for Flu7-300, and 400 °C for Flu7-400. The molar ratio of $Fe(acac)_3$:HF during the synthesis of the precursor was 1:7.

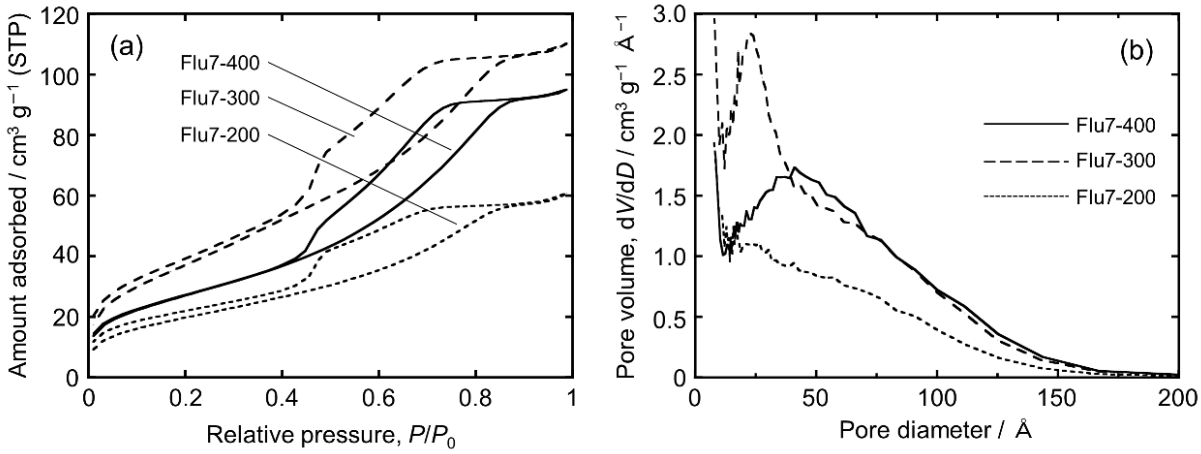

Fig. 5 (a) Nitrogen adsorption–desorption isotherms and (b) pore-size distributions of the FeF_3 products. Fluorination temperatures were 200 °C for Flu7-200, 300 °C for Flu7-300, and 400 °C for Flu7-400. The molar ratio of $Fe(acac)_3$:HF for the synthesis of the precursor was 1:7.

2.2.3 Charge–discharge property

The Flu7-300 sample with the largest surface area was selected as a positive electrode material for further electrochemical measurements. Electrochemical behavior of the commercially available FeF_3 (S-FeF_3) was also investigated for comparison.

The XRD patterns of S-FeF_3 and Flu7-300 are shown in Fig. 6a. The S-FeF_3 sample is highly crystalline with sharp peaks assigned to the rhombohedral FeF_3. Some weak diffraction peaks assigned to the trihydrate of FeF_3, formed during the measurement, were also observed. Nitrogen adsorption–desorption isotherm of S-FeF_3 is shown in Fig. 6b. The S-FeF_3 sample possesses very low adsorption capacity and its BET surface area is calculated to be 4.8 $m^2\ g^{-1}$ that is smaller than the value for Flu7-300 (140 $m^2\ g^{-1}$). Their particle morphologies were observed by field-emission scanning microscopy (FE-SEM) as shown in Fig. 7. Although S-FeF_3 is highly crystalline with crystal edges on the particle, Flu7-300 shows irregular-shape with mesopores. The particle size is around 200–300 nm for S-FeF_3 and 50–100 nm for Flu7-300. The pore size on the surface of Flu7-300 is around or below 20 nm, consistent with the pore size distribution shown in Fig. 5b.

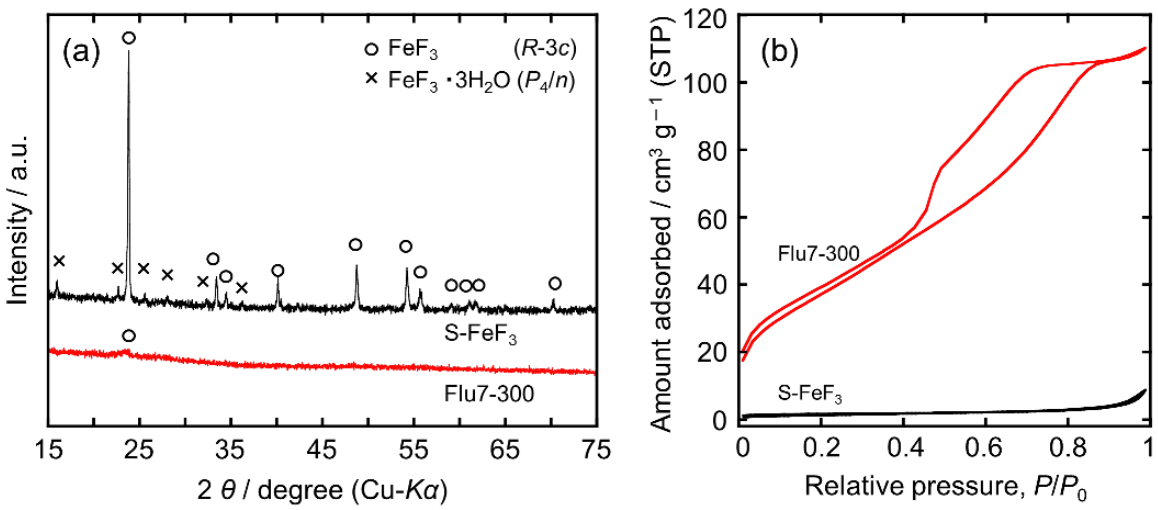

Fig. 6 (a) X-ray diffraction patterns and (b) nitrogen adsorption–desorption isotherms of the commercial FeF_3 (S-FeF_3) and the synthesized FeF_3 (Flu7-300).

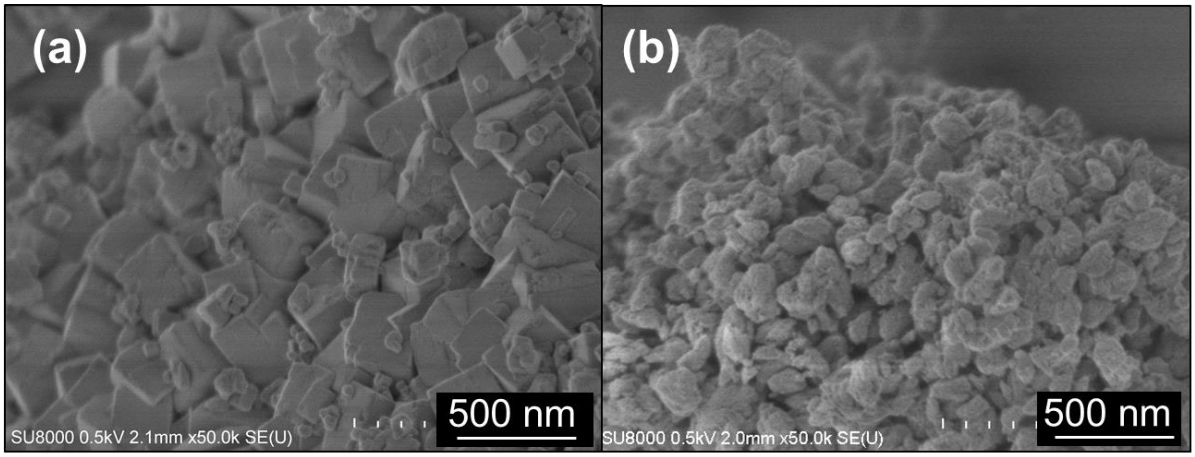

Fig. 7 Field emission-scanning electron microscopic images of (a) the commercial FeF_3 (S-FeF_3) and (b) the synthesized FeF_3 (Flu7-300).

Electrochemical properties of S-FeF_3 and Flu7-300 were investigated by galvanostatic charge–discharge tests using a two-electrode cell. Charge–discharge conditions were fixed at a current density of 71.2 mA g^{-1} with cut-off voltages of 1.0 and 4.5 V. The initial charge–discharge curves for S-FeF_3 and Flu7-300 are shown in Fig. 8a. In the initial discharge, S-FeF_3 showed a

discharge capacity of ca. 150 mAh g^{-1} in the voltage range of 2.0–4.5 V where only the insertion reaction occurs whereas Flu7-300 shows a lower capacity below 100 mAh g^{-1} in this voltage range. This difference is explained by the lower crystallinity of Flu7-300 (see Fig. 6a), which is consistent with the report by Yabuuchi *et al*. that the cycleabilty and rate performance in this voltage range were improved by increasing crystallinity of FeF_3 [5]. Although Flu7-300 shows the low capacity for the insertion reaction, the conversion reaction occurred at a higher potential than that of S-FeF_3. The whole initial discharge capacity of Flu-300 is 676 mAh g^{-1} that exceeds the capacity observed for S-FeF_3 (510 mAh g^{-1}) and is close to the theoretical capacity of FeF_3 (712 mAh g^{-1}). These results are considered to result from the low crystallinity and high surface area of Flu7-300, which realizes the high reactivity in the conversion reaction. Cycleabilities of S-FeF_3 and Flu7-300 are shown in Fig. 8b. Although Flu7-300 exhibits a higher initial discharge capacity, its capacity retention is inferior to that of S-FeF3 during 15 cycles. This may result from the isolation of the active material from electric conduction paths during cycling, which is enhanced by the high surface area and porosity of Flu7-300. Although FeF_3 does not largely change in volume during the charge–discharge process (29.16 cm^3 mol^{-1} for FeF_3 and 36.59 cm^3 mol^{-1} for 3LiF + Fe), the volume change would cause the electric isolation if the amount of polytetrafluoroethylene (PTFE) binder was not enough to ensure the stable contacts between the active material and conductive additive.

A positive electrode with a larger amount of PTFE binder (10 wt% of PTFE) was prepared to confirm the effect of the amount of the binder. Charge–discharge curves for the Flu7-300 electrodes with 5 and 10 wt% of PTFE are shown in Fig. 9a and Fig. 9b, respectively. Large capacity degradation is still observed during the first two cycles for the electrode containing 10 wt% of PTFE, however, the larger capacity for the insertion reaction above 2.0 V is preserved compared to the case of the electrode with 5 wt % of PTFE during 25 cycles. As a result, as shown in Fig. 9c, the high reversible capacity is observed for the composite electrode with 10 wt% of PTFE. The

improvement of the capacity retention arises from the better binding ability based on the larger amount of PTFE binder, leading to give a better contacts between the FeF_3 active material and conductive agents during cycling.

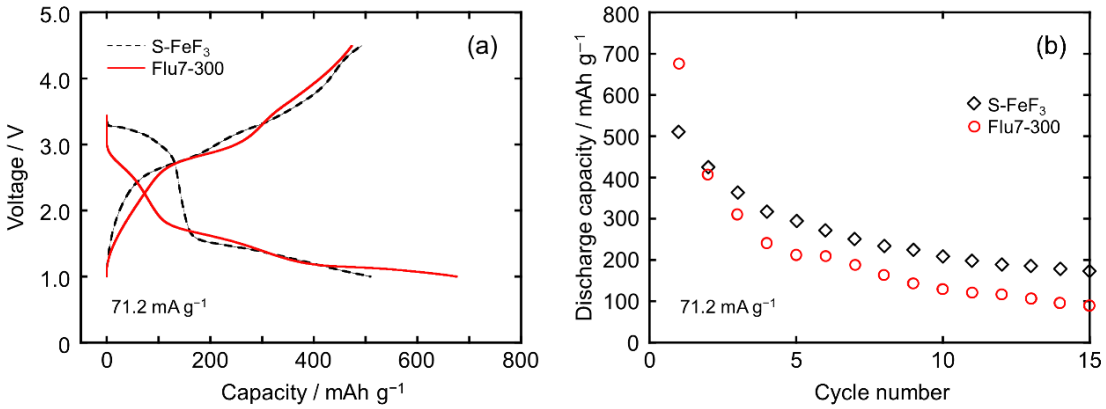

Fig. 8 (a) Initial charge–discharge curves and (b) cycleabilities for the commercial FeF_3 (S-FeF_3) and the synthesized FeF_3 (Flu7-300).

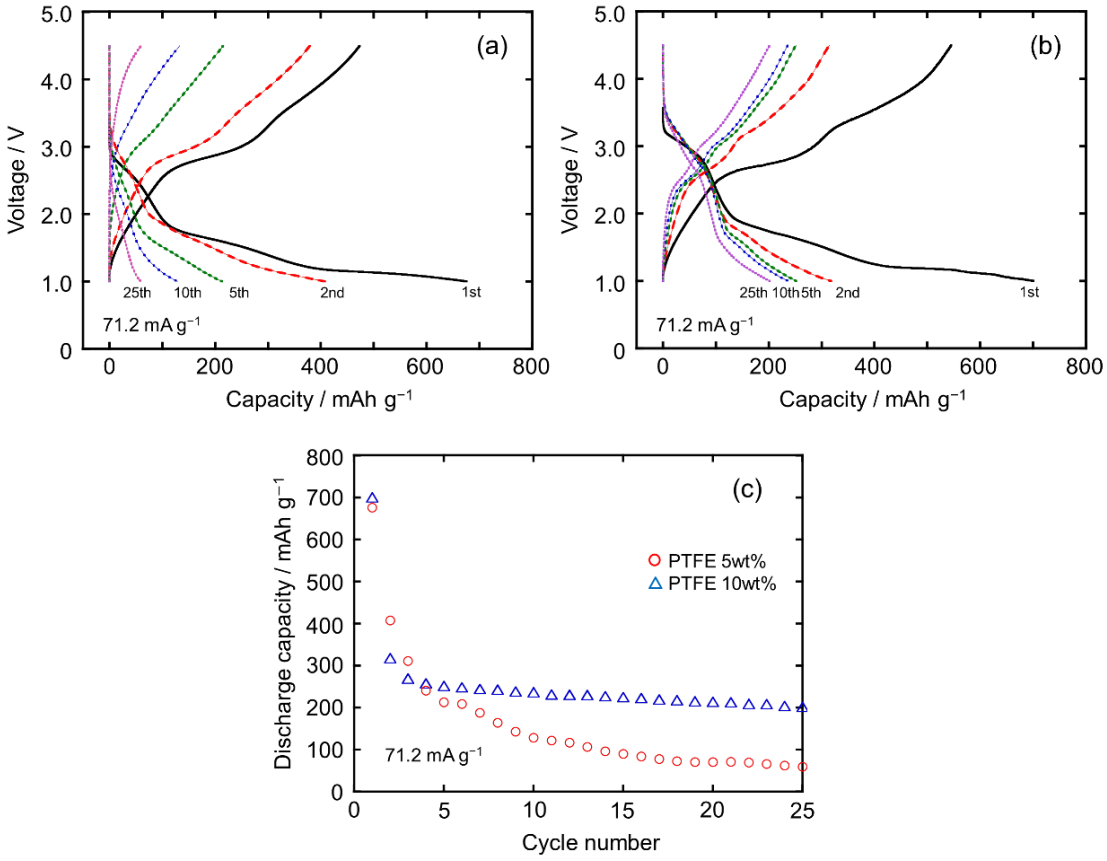

Fig. 9 Charge–discharge curves for the Flu7-300 electrodes in which the amount of PTFE binder is (a) 5 wt% and (b) 10 wt%, and (c) cycleability of the electrodes during 25 cycles.

3. Conclusions

FeF_3 with low crystallinity and high surface area was synthesized by a fluorolysis method in order to improve the performance of the conversion reaction as a positive electrode material of lithium ion battery. The FeF_3 was synthesized under the different synthetic conditions such as HF ratio in the first reaction step and fluorination temperature in the second reaction step in the fluorolysis method. It was revealed that a high HF ratio lead to high surface area and high crystalline structure. Fluorination at high temperature effectively removed carbon-containing impurities from the FeF_3 products. The highest surface area was realized by fluorination at 300 °C. The FeF_3 prepared by the fluorolysis method showed a low capacity for the insertion reaction owing to its low crystallinity. However, the conversion reaction occurred with a high capacity at a higher

potential than the crystalline FeF_3. The cycleability of the FeF_3 was improved by increasing the ratio of the PTFE binder in an electrode, preventing the FeF_3 active materials from the electric isolation during cycling.

4. Experimental

4.1 Apparatus

Moisture sensitive materials were handled in an open dry chamber under a dry-air atmosphere and/or in a glove box under a dry-Ar atmosphere. Corrosive materials such as hydrogen fluoride and elemental fluorine were handled in a reaction line made of corrosion-resistant stainless steel pipes (SS-316, 1/2-inch o.d.) and valves with a polychlorotrifluoroethylene stem tip. The reaction line was connected to a rotary vacuum pump through a chemical trap filled with soda lime and a glass cold trap cooled by liquid nitrogen connected in series. The pressure in the line was monitored by Bourdon and Pirani gauges.

4.2 Reagents

Anhydrous hydrgen fluoride (HF, Daikin Industries Co. Ltd., purity > 99%)) was dried over dipotassium hexafluoronickelate (Ozark-Mahoning Elf Atochem North America, Inc.) in a tetrafluoroethylene-perfluoroalkylvinylether copolymer (PFA) reactor prior to use. Diluted elemental fluorine was prepared by mixing pure elemental fluorine (F_2, Daikin Industry Co. Itd., purity > 99.7%) and argon (Ar, Kyoto Teisan K.K., purity > 99.998%) in the molar ratio of 1:4 and stored in a stainless steel cylinder. Iron(III) acetylacetonate ($Fe(acac)_3$, Sigma-Aldrich, Inc., purity > 99.9%), methanol (MeOH, Wako Pure Chemical Industries, Ltd., purity > 99.8%, water content < 10 ppm), and iron(III) fluoride (S-FeF_3, Soekawa Chemical Co., Ltd., purity > 97%) were used as received.

4.3 Preparation of a FeF_3 precursor

The synthesis of FeF_3 was performed based on literature [33]. To obtain a precursor of FeF_3, MeOH solutions of $Fe(acac)_3$ (0.18 M) and HF (7.2 M) were separately loaded in PFA reactors. The two reactors were connected with a T-shaped PTFE union with a stainless steel valve. The solution of HF was slowly transfered to the other arm in the 1:3, 1:5, or 1:7 molar ratio of $Fe(acac)_3$ and HF, and the solution was sttired for 6 days. A FeF_3 precursor, $FeF_{3-x}(acac)_x$, was obtained by evacuation of the solution at room temperature until the liquid disappeared and at 45 °C for 2 days.

4.4 Fluorination by elemental fluorine

The precursor, $FeF_{3-x}(acac)_x$, was loaded in a nickel boat which was placed a nickel tube and heat-treated under a flow of argon at 200 °C for 2 hours, followed by fluorination under a flow of the diluted elemental fluorine (F_2 / Ar = 1 / 4) at 200, 300, or 400 °C for 2 hours. The flow rate was controlled as 25 mL min^{-1} by a mass flow monitor and controller, HFC-D-302 (Teledyne Hasting Instruments).

4.5 Preparation of positive electrodes

The FeF_3 active material was dry-milled with acetylene black (AB, Wako Pure Chemical Industries, Ltd., purity > 99.99%) in the weight ratio of 70:25 in zirconia vials with zirconia balls by using a planetary ball mill, PLP-7 (Fritsch Japan Co., Ltd) at 600 rpm for 12 hours to form FeF_3/AB composites as described in the literature [15]. Polytetrafluoroethylene (Sigma-Aldrich, Inc., powdery) was used as a binder for a positive electrode. The FeF_3/AB composite and PTFE were well mixed in an agate mortar in the weight ratio of 95:5 or 90:10 with an agate pestle and mortar until it became a homogeneous thin sheet. The sheet was pressed on aluminum mesh under the pressure of 3 t cm^{-2} to form a positive electrode disk.

4.6 Charge–discharge test

Galvanostatic charge–discharge tests were performed using 2032 coin-type cells. The cells were assembled in the glove box using a 1 M $LiPF_6$/EC+DMC (1:1 in volume, Kishida Chemical Co. Ltd., EC = ethylenecarbonate and DMC = dimethylcarbonate) electrolytic solution, glass fiber filter separator (Whatman, GF/A, 260μm in thickness), and metal lithium foil counter electrode pressed on a stainless steel plate.

4.7 X-ray diffraction (XRD)

Samples for XRD were loaded on a glass sample holder and diffraction patterns were recorded by a powder X-ray diffractometer, Ultima IV (Rigaku Corp., Cu-*Kα* radiation, 40 kV-40 mA). Air sensitive samples were sealed in an air-tight cell with beryllium windows (Rigaku Corp.) under a dry argon atmosphere.

4.8 Field emission scanning electron microscope (FE-SEM)

Morphology of the samples was observed by field-emission scanning electron microscope (FE-SEM; Hitachi, SU-8020). Samples were fixed on an electron-conductive carbon sheet without coating by a conductive additive. The image was obtained with a low accelerating voltage of 0.5 kV to avoid the charge-up of the sample.

4.9 Nitrogen adsorption analysis

Nitrogen adsorption analysis was performed by Tristar II 3020 (Shimadzu Corp.) to evaluate surface area and pore-size distribution of the samples. The surface area and pore size distribution were evaluated by the methods of Brunauer–Emmett–Teller (BET) [33] and Barrett–Joyner–Halenda (BJH) [34], respectively.

Acknowledgements

This work was supported by JSPS Grant-in-Aid for Young Scientists (B) Grant Number 24750181.

Figure captions

Fig. 1 X-ray diffraction patterns of the FeF_3 precursors. The molar ratio of $Fe(acac)_3$:HF is 1:3 for Pre3, 1:5 for Pre5, and 1:7 for Pre7.

Fig. 2 X-ray diffraction patterns of the FeF_3 products. The molar ratio of $Fe(acac)_3$:HF is 1:3 for Flu3-200, 1:5 for Flu5-200, and 1:7 for Flu7-200. The fluorination temperature is 200 °C.

Fig. 3 (a) Nitrogen adsorption–desorption isotherms and (b) pore-size distributions of the FeF_3 products. The molar ratio of $Fe(acac)_3$:HF is 1:3 for Flu3-200, 1:5 for Flu5-200, and 1:7 for Flu7-200. The fluorination temperature is 200 °C.

Fig. 4 X–ray diffraction patterns of the FeF_3 products. The fluorination temperature is 200 °C for Flu7-200, 300 °C for Flu7-300, and 400 °C for Flu7-400. The molar ratio of $Fe(acac)_3$:HF is 1:7.

Fig. 5 (a) Nitrogen adsorption–desorption isotherms and (b) pore-size distributions of the FeF_3 products. The fluorination temperature is 200 °C for Flu7-200, 300 °C for Flu7-300, and 400 °C for Flu7-400. The molar ratio of $Fe(acac)_3$:HF is 1:7.

Fig. 6 (a) X-ray diffraction patterns and (b) nitrogen adsorption–desorption isotherms of the commercial FeF_3 (S-FeF_3) and the synthesized FeF_3 (Flu7-300).

Fig. 7 Field emission-scanning electron microscopic images of (a) the commercial FeF_3 (S-FeF_3) and (b) the synthesized FeF_3 (Flu7-300).

Fig. 8 (a) Initial charge–discharge curves and (b) cycleabilities for the commercial FeF_3 (S-FeF_3) and the synthesized FeF_3 (Flu7-300).

Fig. 9 Charge–discharge curves for the Flu7-300 electrodes in which the amount of PTFE binder is (a) 5 wt% and (b) 10 wt%, and (c) cycleability of the electrodes during 25 cycles.

References

[1] J.B. Goodenough, Y. Kim, *Chem. Mater.*, **22** (2010) 587-603.

[2] V. Etacheri, R. Marom, R. Elazari, G. Salitra, D. Aurbach, *Energy Environ. Sci.*, **4** (2011) 3243-3262.

[3] J.B. Goodenough, K.-S. Park, *J. Am. Chem. Soc.*, **135** (2013) 1167-1176.

[4] K. Mizushima, P.C. Jones, P.J. Wiseman, J.B. Goodenough, *Mat. Res. Bull.*, **15** (1980) 783-789.

[5] J.N. Reimers, J.R. Dahn, *J. Electrochem. Soc.*, **139**(8) (1992) 2091-2097.

[6] A.K. Padhi, K.S. Nanjundaswamy, J.B. Goodenough, *J. Electrochem. Soc.*, **144**(4) (1997) 1188-1194.

[7] H. Arai, S. Okada, Y. Sakurai, J. Yamaki, *J. Power Sources*, **68** (1997) 716-719.

[8] F. Badway, N. Pereira, F. Cosandey, G.G. Amatucci, *J. Electrochem. Soc.*, **150** (2003) A1209-A1218.

[9] F. Badway, F. Cosandey, N. Pereira, G.G. Amatucci, *J. Electrochem. Soc.*, **150** (2003) A1318-A1327.

[10] H. Li, G. Richter, J. Maier, *Adv. Mater.*, **15** (2003) 736-739.

[11] R.E. Doe, K.A. Persson, Y.S. Meng, G. Ceder, *Chem. Mater.*, **20** (2008) 5274-5283.

[12] M. Nishijima, I.D. Gocheva, S. Okada, T. Doi, J. Yamaki, T. Nishida, *J. Power Sources*, **190** (2009) 558-562.

[13] N. Yamakawa, M. Jiang, B. Key, C.P. Grey, *J. Am. Chem. Soc.*, **131** (2009) 10525-10536.

[14] T. Li, L. Li, Y.L. Cao, X.P. Ai, H.X. Yang, *J. Phys. Chem.*, **114** (2010) 3190-3195.

[15] N. Yabuuchi, M. Sugano, Y. Yamakawa, I. Nakai, K. Sakamoto, H. Muramatsu, S. Komaba, *J. Mater. Chem*., **21** (2011) 10035-10041.

[16] L. Li, F. Meng, S. Jin, *Nano Lett.*, **12** (2012) 6030-6037.

[17] P. Liu, J.J. Vajo, J.S. Wang, W. Li, J. Liu, *J. Phys. Chem.*, **116** (2012) 6467-6473.

[18] J. Liu, Y. Wan, W. Liu, Z. Ma, S. Ji, J. Wang, Y. Zhou, P. Hodgson, Y. Li, *J. Mater. Chem*., **1** (2013) 1969-1975.

[19] C. Li , X. Mu, P.A. Aken, J. Maier, *Adv. Energy Mater.*, **3** (2013) 113-119.

[20] R. Ma, M. Wang, P. Tao, Y. Wang, C. Cao, G. Shan, S. Yang, L. Xi, J.C.Y. Chung, Z. Lu, *J. Mater. Chem.*, **1** (2013) 15060-15067.

[21] S.-T. Myung, S. Sakurada, H. Yashiro, Y.-K. Sun, *J. Power Sources*, **223** (2013) 1-8.

[22] Q. Chu, Z. Xing, J. Tian, X. Ren, A.M. Asiri, A.O. Al-Youbi, K.A. Alamry, X. Sun, *J. Power Sources*, **236** (2013) 188-191.

[23] M. Duttine, D. Dambournet, N. Penin, D. Carlier, L. Bourgeois, A. Wattiaux, KW. Chapman, P.J. Chupas, H. Groult, E. Durand, A. Demourgues, *Chem. Mater.*, **26** (2014) 4190-4199.

[24] L.D. Carlo, D.E. Conte, E. Kemnitz, N. Pinna, *Chem. Commun.*, **50** (2014) 460-462.

[25] J.K. Ko, K.M. Wiaderek, N. Pereira, T.L. Kinnibrugh, J.R. Kim, P.J. Chupas, K.W. Chapman, G.G. Amatucci, *ACS Appl. Mater. Interfaces*, **6** (2014) 10858-10869.

[26] H.J. Tan, H.L. Smith, L. Kim, T.H. Harding, S.C. Jones, B. Fultz, *J. Electrochem. Soc.*, **161**(3) (2014) A445-A449.

[27] E. Kemnitz, U. Groß, S. Rüdiger, C.S. Shekar, *Angew. Chem. Int. Ed.*, **42** (2003) 4251-4254.

[28] S.K. Ruediger, U. Groß, M. Feist, H.A. Prescott, S.C. Shekar, S.I. Troyanov, E. Kemnitz, *J. Meter. Chem.*, **15** (2005) 588-597.

[29] S. Rüdiger, G. Eltanany, U. Groß, E. Kemnitz, *J. Sol-Gel Sci. Tech.*, **41** (2007) 299-311.

[30] S. Wuttke, G. Scholz, S. Rüdiger, E. Kemnitz, *J. Mater. Chem.*, **17** (2007) 4980-4988.

[31] S. Wuttke, A. Vimont, J.C. Lavalley, M. Daturi, E. Kemnitz, *J. Phys. Chem.*, **114** (2010) 5113-5120.

[32] T. Patil, PhD thesis of Humboldt-Universität zu Berlin, 2008.

[33] S. Brunauser, P.H. Emmett, E. Teller, *J. Am. Chem. Soc.*, **60** (1938) 309-319.

[34] E.P. Barrett, L.G. Joyner, P.H. Halenda, *J. Am. Chem. Soc*., **73** (1951) 373-380.